Article

Angle of Inclination of Tank-Treading Red Cells: Dependence on Shear Rate and Suspending Medium

Thomas M. Fischer[1,*] and Rafal Korzeniewski[1]
[1]Department of Physiology, Rheinisch Westfälische Technische Hochschule Aachen University, Aachen, Germany

ABSTRACT Red cells suspended in solutions much more viscous than blood plasma assume an almost steady-state orientation when sheared above a threshold value of shear rate. This orientation is a consequence of the motion of the membrane around the red cell called tank-treading. Observed along the undisturbed vorticity of the shear flow, tank-treading red cells appear as slender bodies. Their orientation can be quantified as an angle of inclination (θ) of the major axis with respect to the undisturbed flow direction. We measured θ using solution viscosities (η_0) and shear rates ($\dot{\gamma}$) covering one and three orders of magnitude, respectively. At the lower values of η_0, θ was almost independent of $\dot{\gamma}$. At the higher values of η_0, θ displayed a maximum at intermediate shear rates. The respective maximal values of θ increased by ~10° from 10.7 to 104 mPas. After accounting for the absent membrane viscosity in models by using an increased cytoplasmic viscosity, their predictions of θ agree qualitatively with our data. Comparison of the observed variation of θ at constant $\dot{\gamma}$ with model results suggests a change in the reference configuration of the shear stiffness of the membrane.

INTRODUCTION

Blood is a suspension of blood cells in blood plasma. The volumetric concentration of blood cells is called hematocrit (Hct). By far the biggest contribution to the Hct is red cells. They transport oxygen from the lungs to the other organs and return with carbon dioxide. During their passage through the vasculature, they are deformed in many ways. These deformations are facilitated by the unique design of the red cell: a closed, nonspherical membrane that encloses a liquid cytoplasm.

The elastic and viscous properties of the membrane have been studied extensively. Its elastic properties are described by two quantities: 1) a reference configuration (RC) in which no elastic energy is stored in the material in question and 2) a stiffness quantifying the increase in elastic energy upon deviation from the RC. Locally, the RC can be considered as the shape of a small piece of membrane conceptually excised and allowed to relax. Because the red cell membrane is closed, its parts are in general not in their respective RC. A global RC, i.e., a shape free of stresses (1) and/or bending moments, is a special case. A way to describe the distribution of local RCs in the general case has been suggested (2).

From a mechanical point of view, the red cell membrane consists of two layers—a phospholipid bilayer, and the membrane skeleton, which is a network of proteins underlying the bilayer. The bilayer endows the red cell with constant surface area and constant volume and the membrane with bending elasticity. The bilayer behaves as a liquid. Accordingly, the RC for bending is a single value, the spontaneous curvature (c_0). The skeleton provides elastic and viscous properties to the membrane. As an RC, a stress-free shape has been chosen traditionally.

When whole blood (Hct $\approx$ 0.45) is subjected to high shear rates ($\dot{\gamma}$) in vitro and observed along the undisturbed gradient, the red cell shapes are irregular due to crowding but show, on average, an elongation parallel to the direction of flow (3). Upon reducing the Hct to simplify the boundary conditions, the red cells are deformed but no longer elongated (3). However, the elongation can be recovered without crowding by increasing the viscosity of the suspending medium, thus allowing us to observe the red cell shape and its flow behavior in great detail.

Such experiments showed two main modes of motion: At low shear rates, the red cells rotate, essentially preserving their resting shape. This mode of motion is called "tumbling" (TB). Above a threshold value in shear rate, the red cells do not rotate but assume an essentially steady-state orientation. This mode is characterized by a two-dimensional flow of the membrane around the oriented red cell, in a motion that has been termed "tank-treading" (TT) (4). Keller and Skalak (5) showed that the steady-state orientation of TT red cells is due to a balance of two opposing moments. One moment results from the vorticity of the shear flow, the other one from the tank-tread motion of the membrane.

Observed along the undisturbed vorticity of the shear flow, TT red cells appear as slender bodies. Their orientation can be quantified by an angle of inclination (θ) of the long

Submitted October 22, 2014, and accepted for publication January 23, 2015.

*Correspondence: thmfischer@gmail.com
Thomas M. Fischer's present address is Laboratory for Red Cell Rheology, Krummer Weg 20, 52134 Herzogenrath, Germany.

Editor: Reinhard Lipowsky.

0006-3495/15/03/1352/9 $2.00
http://dx.doi.org/10.1016/j.bpj.2015.01.028

axis (L) with respect to the undisturbed flow direction. It was shown that θ displays an oscillation about a mean value, a phenomenon called "swinging" (SW) (6). An oscillation in shear elastic energy (amplitude $= E_0$) during TT due to an RC with nonspherical symmetry was shown to be the origin of SW (7). Our work provides statistically firm data on instantaneous values of θ covering large ranges in suspending viscosity (η_0) and $\dot{\gamma}$. For technical reasons, SW is not recorded, but accounted for indirectly.

It has been shown theoretically that $\theta \neq 0$ leads to an asymmetry of the diffraction pattern obtained along the undisturbed gradient (8). However, this asymmetry is too small to determine θ with precision. We observed red cells microscopically along the undisturbed vorticity of a Poiseuille flow. Besides θ, we measured L and the red cell thickness (D) and use these data for a comparison with model calculations from the literature. Based on this comparison, our data can be used to tune the physical assumptions of future refinements of these models.

MATERIALS AND METHODS

Dextran solutions

The sources of dextran are shown in Table 1. Dextran solutions were prepared as reported previously in Fischer (9). In short, dextrans of different molecular weights were dissolved in water. The concentrations (w/v) were the same for all dextrans as controlled by refractometry (Abbe; Zeiss, Oberkochen, Germany). Electrolytes were added as a stock solution of PBS (PBS-Dulbecco 10×; Biochrome, Berlin, Germany). The amount of electrolyte was chosen to preserve the volume the red cells have in blood plasma. The viscosity of these solutions was measured in a rolling ball viscometer (Anton Paar, Graz, Austria) at 23°C (Table 1). To counteract shape changes of red cells, either the echinocytic agent Sulfobetaine SB 12 (concentration 0–10 μM; Stricker, Tutzing, Germany) or the stomatocytic agent human albumin (concentration 0–4 mg/100 mL; Sigma-Aldrich, Munich, Germany) were added to the dextran solutions.

Preparation of red cell suspensions

Blood was obtained on a voluntary basis from regular donors at the local blood bank and aspirated into heparin-containing vacutainers. A quantity of 1000 μL of whole blood was pipetted into an Eppendorf vial, put on ice for 15 min, and then centrifuged at 5600 g for 4 min. Supernatant plasma was removed for later addition. Due to the preceding cooling and the rewarming during centrifugation, the buffy coat was rather solid and floated above the red cell column. Therefore it could be aspirated with minimal loss of red cells. Finally, plasma was added to obtain a red cell concentration (v/v) of ~0.5. This suspension was diluted in three steps 5×10^{-4} times with dextran solution to make the final suspension.

TABLE 1 Dextrans used in this study

Dextran	MW/kDa	Company	Lot No.	Viscosity/mPas
T 40	41	Pharmacia	2771	10.7
100	100	Serva	B	23.9
500	497	Serva	G9	55.9
T 2000	2000	Pharmacia	8122	104

MW denotes the average molecular weight. Dextran T 2000 was dialyzed and freeze-dried before use. Viscosities were measured at 23°C.

Protocol

See Sections S1.1, S1.2, and S1.4 in the Supporting Material for details. In short, the shape of TT red cells was observed microscopically while flowing through a glass capillary (luminal diameter, 975 μm). The flow was driven at constant pressure from a reservoir and varied by more than three orders of magnitude using different resistances at the outflow. The focus of the microscope was set onto the midplane of the capillary. To do this in a reproducible fashion, the velocity distribution parallel and at right angles to the optical axis of the microscope was determined in preliminary experiments.

The shape of the red cells was frozen by flash illumination and recorded with an interlaced black-and-white TV camera. A double-flash method exposing separately the two half-frames of the camera with variable distance of the two flashes allowed determination of the velocity of flowing objects. The experiments were performed at room temperature (23°C) and completed within 4 h after blood withdrawal. Seven blood samples and totaling 36,519 red cells were evaluated.

Evaluation

See Section S1.3 in the Supporting Material for details. In short, the images of the recordings were processed by custom-made software. A grayscale threshold converted half-tone images into binary images; i.e., solid objects on open background. The contour of these solid objects defined their shape. The values of θ were obtained by determination of the principal axes of all pixels inside and including the contour. The values L and D were determined as the lengths of the segments of the principal axes lying within the outer edge of the contour.

In selecting objects for further evaluation, two threshold values for the quality of focus (see Section S1.3, item 7, in the Supporting Material) were applied. To assess the shape of the cross sections, a higher threshold value was necessary than for the determination of θ (see Fig. 1, a and c) .

The lengths of subaxes parallel to the minor axis were used to obtain a measure of the deviation from the symmetry of the binary images. Fig. 1, b and d, shows the same images as in Fig. 1, a and c, but overlaid with the principal axes (*open*), then the subaxes (*shaded*), and finally the contour (*solid*).

Red cells react sensitively to small changes in the composition of the suspending medium (10). In the experiments, such changes could not completely be avoided. At low elongations, the resulting curvatures of the cell contour are still noticeable. Such cells were excluded by applying thresholds for several asymmetry measures (see Section S1.3, item 9, in the Supporting Material). With increasing shear rates, isotropic membrane tensions pull the membrane locally flat. Such cells gave no signature of their resting shapes and were included in the study.

The apparent radial position of flowing objects was calculated from their position within the image and the position of the capillary relative to the

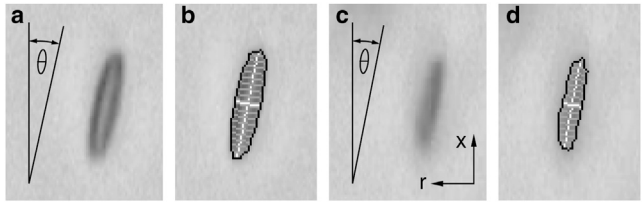

FIGURE 1 (a and c) Microscopic images of two TT red cells, $\eta_0 = 23.9$ mPas, $\dot{\gamma} = 32.4$/s. The angle of inclination (θ), as determined by image processing, is shown; x and r indicate the direction and the gradient of the undisturbed shear flow, respectively. (a) This cell is in focus, thus allowing us to determine the dimensions of the cross section as well as θ. (c) This cell is somewhat out of focus but still allows us to determine θ. (b and d) Same images as a and c, respectively, overlaid first with the principal axes (*open*), then with the subaxes (*shaded*), and finally with the contour (*solid*). The height of the images corresponds to 23.1 μm.

optical axis of the microscope (see Section S1.5 in the Supporting Material). The actual radial position was derived from the apparent position based on a geometric optics calculation, which accounted for the refraction of light at the curved surfaces between glass and dextran solution (see Section S1.6 in the Supporting Material).

Cells closer to the wall than 50 μm were excluded from the evaluation so that essentially their behavior in an unbounded shear flow was observed. The shear rate to which a flowing particle was subjected was determined from its actual radial position, its velocity, and the luminal radius of the capillary (see Section 1.8 in the Supporting Material). A precondition for this approach is the absence of slip of TT red cells with respect to the undisturbed fluid flow. This absence was demonstrated in extra experiments (see Section S1.7 in the Supporting Material).

RESULTS AND DISCUSSION

Angle of inclination (θ)

In a previous study (11), these data were used to establish a phase diagram separating the two modes TB and TT. A threshold shear rate ($\dot{\gamma}_t$) above which TT was observed for the majority of the population was determined for each blood sample and each value of η_0. In the following, only data with $\dot{\gamma} > \dot{\gamma}_t$ are presented.

Typical images of red cells observed along the undisturbed vorticity are shown in Fig. 1. Cells as in Fig. 1 *a* are in focus, thus allowing us to determine the dimensions of the cross section as well as θ. Cells as in Fig. 1 *c* are somewhat out of focus and are used to determine only θ.

Fig. 2 shows an example of the dependence of θ on $\log(\dot{\gamma})$. The data come in groups, each group belonging to a certain flow rate. A group covers the $\dot{\gamma}$ -range encompassed by the radial range of the microscopic image.

Fig. 3 shows θ-values after log-binning and averaging of all seven blood samples tested. At $\eta_0 = 10.7$ mPas (Fig. 3 *a*), θ is essentially independent of $\log(\dot{\gamma})$. With increasing η_0 (Fig. 3, *b–d*), θ first increases with rising $\log(\dot{\gamma})$ to reach a maximum and then decreases. This nonmonotonic behavior of θ is discussed in Section S2.2 in the Supporting Material. In Fig. S7, the single values of all samples are lumped together and are shown for each value of η_0. Fit-functions were chosen pragmatically to derive mean values. The maximum value of θ rises monotonically with η_0 (Figs. 3 and S7). It increases from 9° to 19° for η_0 from 10.7 to 104 mPas.

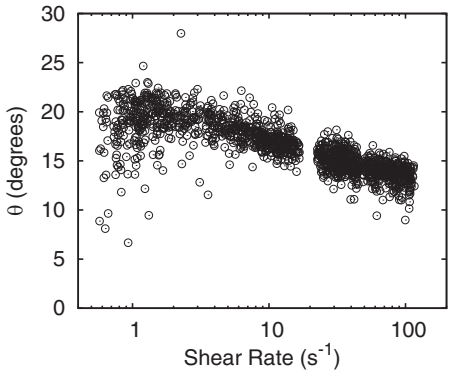

FIGURE 2 Angle of inclination (θ) of TT red cells versus shear rate. Results of individual red cells (sample 7, $\eta_0 = 104$ mPas).

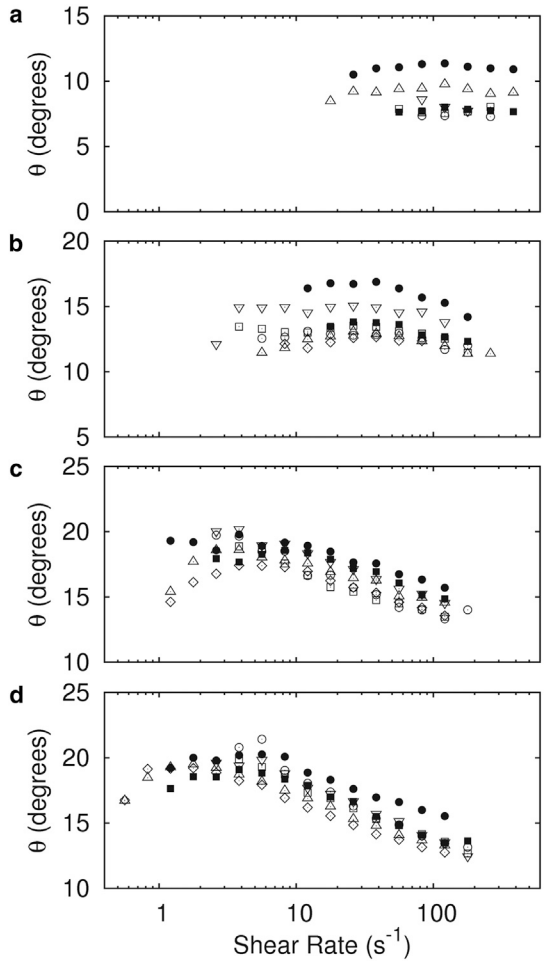

FIGURE 3 Angle of inclination (θ) of TT red cells versus shear rate. Population-averaged results of seven blood samples: 1 (*open circle*), 2 (*open square*), 3 (*open down-triangle*), 4 (*solid circle*), 5 (*solid square*), 6 (*open diamond*), and 7 (*open up-triangle*), with η_0 in mPas, as (*a*) 10.7, (*b*) 23.9, (*c*) 55.9, and (*d*) 104.

Distributions of θ

Two effects determine the distribution of the experimental points in θ-direction. The first is SW (effect A). The range of θ-values assumed during SW is called swinging range (SWR) hereafter. The second is that the time-averaged values of individual red cells ($\langle\theta\rangle$) are expected to vary due to the distribution of the mechanical properties within the red cell population (effect B). Both effects merge into a convolution of a normal distribution (effect B) and the residence time in subintervals of the SWR (effect A).

It could be argued that "vacillating-breathing" (VB) also contributes to the observed dispersion of θ. In a model for almost spherical vesicles, VB was first described in Misbah

(12) as SW with large SWR at $\langle\theta\rangle = 0$. Later, VB was reported in red cell models with biconcave stress-free shapes (13,14). These two studies show severe membrane buckling during TT, which is not observed in experiments with biconcave red cells (T.M.F., personal observation). Therefore, VB cannot be used as an explanation for the extremely small percentage of θ-values at ~0. Instead, we consider these data to be caused by indeformable TB cells.

The experimental distributions were determined for each blood sample and each value of η_0 in three steps.

1. The observed θ-values were sorted into six $\dot{\gamma}$-bins per decade. The lowest $\dot{\gamma}$-bin contains $\dot{\gamma}_t$ and is therefore in general only partly filled. It was united with the adjacent $\dot{\gamma}$-bin. Altogether, 227 $\dot{\gamma}$-bins contained between 61 and 569 θ-values.
2. The θ-values in each $\dot{\gamma}$-bin were corrected to the center of the respective $\dot{\gamma}$-bin according to the sample-specific dependence of θ on $\log(\dot{\gamma} \times \mathrm{s})$.
3. In each $\dot{\gamma}$-bin, the corrected θ-values were sorted into θ-bins and a histogram was generated.

Most histograms looked bell-shaped, plus a small percentage of outliers. Two examples are shown in Fig. 4, *c* and *d* (*shaded columns*). Each histogram was fitted by a normal distribution (mean value $= \mu_e$ and $SD = \sigma_e$) (see Fig. 4, *c* and *d*, *continuous lines*). The values of σ_e represent the properties of the majority of the population because the outliers have little impact on the fitted normal distribution (see, e.g., Fig. 4 *c*). We will discuss the majority of the values and the outliers separately.

In the following, we use $\dot{\gamma}\eta_0 = \tau$ and $\dot{\gamma}_t\eta_0 = \tau_t$. A semilogarithmic plot of σ_e versus $\dot{\gamma}$ showed great dispersion, which strongly decreased upon plotting versus $\tau - \tau_t$ (Fig. 4 *a*). In this plot, σ_e is greatest close to τ_t and decreases with increasing values of τ. This is interpreted as an influence of SW because we expect the SWR to decrease with increasing red cell elongation due to a decrease of the relative contribution of E_0 to the total elastic energy stored in membrane shear.

The values comprising each histogram were subdivided into two groups. Values of $\theta \notin [\mu_e - 2.58\sigma_e, \mu_e + 2.58\sigma_e]$ were defined as outliers. The rest was considered to belong to the majority of the respective population.

To estimate the contribution of SW in the majority, model convolutions were generated (see Section S2.4 in the Supporting Material). A sinusoidal time dependence of θ during SW was assumed. Its amplitude (A_{SW}) corresponds to SWR/2. Fig. S15 shows the progression of the model convolutions (shaded) upon increasing A_{SW}. These convolutions were fitted with a normal distribution (*blue*) resulting in $SD = \sigma_c$. At low values of A_{SW}/σ_c, the shapes of the model convolutions resemble normal distributions (Fig. S15). Above a ratio of unity, the difference is clearly appreciable.

In the histograms, one would expect a deviation from normality when σ_e is large. But even the distributions of the two top values in Fig. 4 *a*, which are shown in Fig. 4, *c* and *d*, do not show a signature of the convolution. For later use in Previous Experiments and Models without Shape Restrictions, we therefore take σ_e as an upper bound for A_{SW} of the majority of red cells in each $\dot{\gamma}$-bin.

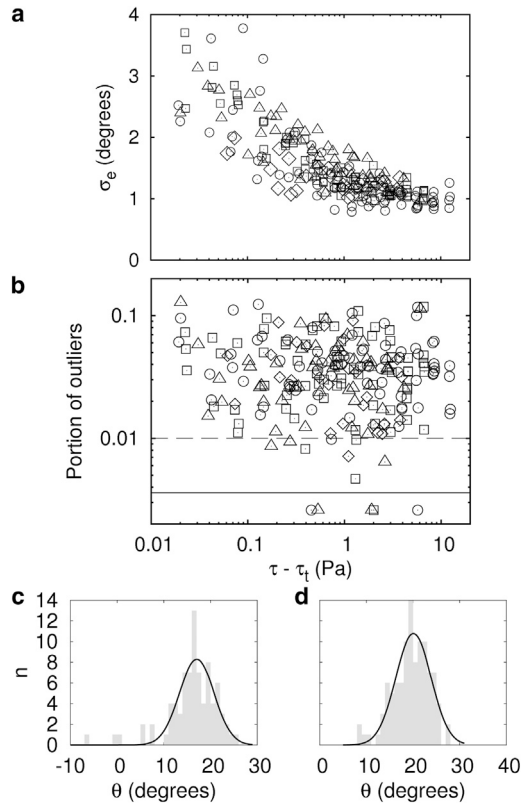

FIGURE 4 Experimental distributions of θ were determined after $\dot{\gamma}$-binning the original data; e.g., Fig. 2. (*a* and *b*) The value η_0 in mPas: 10.7 (*open diamond*), 23.9 (*open up-triangle*), 55.9 (*open square*), and 104 (*open circle*). (*c*) $\eta_0 = 55.9$ mPas, $\dot{\gamma} = 1.62$/s; (*d*) $\eta_0 = 104$ mPas, and $\dot{\gamma} = 3.49$/s. Histograms of two distributions (shown as *shaded columns* in *c* and *d*). Each histogram was fitted with a normal distribution (*continuous line* in *c* and *d*). The SDs of these normal distributions (σ_e) are plotted semilogarithmically versus $\tau - \tau_t$ in *a*. The two top values in *a* correspond to the two examples in *c* and *d*. The portion of the experimental values falling below the 0.5th percentile or above the 99.5th percentile of the respective fitted normal distribution is plotted semilogarithmically versus $\tau - \tau_t$ in *b*. (*Dashed line*) Respective value of a normal distribution. Values of zero are plotted (below the *continuous line*).

With respect to the outliers, we note that in a normal distribution, 1% of the sample is $\notin [\mu_e - 2.58\sigma_e, \mu_e + 2.58\sigma_e]$. In the model convolutions, the percentage is even lower because they fall off more quickly at the rims (see Fig. S15). Fig. 4 *b* shows that in most $\dot{\gamma}$-bins the portion of outliers ranged between 1 and 10%. Interestingly, there is no dependence on $\tau - \tau_t$, suggesting that a small subpopulation exists with values of SWR much greater than that of the majority.

Outstanding values of SWR and thus of E_0 may be caused either by an increase in membrane shear modulus and/or by an RC in shear deviating from that of the majority. An

increase in shear modulus might occur toward the end of the life span of red cells. A deviation in the RC might be due to a nonaverage shear history in the circulation, provided that shear stresses relax by a reorganization of the membrane skeleton.

S-shape

Observed along the vorticity, the symmetry of the undisturbed shear field is that of a rotation by 180°. Particles elongated in flow having exclusively this symmetry have been observed experimentally with fluid drops (15,16) as well as theoretically in capsules (17) and red cell models (13,14,18,19). These shapes resemble an extended letter *S* and are referred to as "S-shapes" hereafter. In TT red cells, S-shapes have as yet not been reported.

To search for S-shapes, the cells of all blood samples and of all values of η_0 were cumulated and binned for *L*. Three symmetries were exploited to find cells with an S-shape: two reflection symmetries with respect to the major and minor axis (*open* in Fig. 6, *b* and *d*) and a rotation by 180°. Cells with a high score for the rotational symmetry and a low score for the reflections were selected. See Section S1.3, item 9 in the Supporting Material, for the method to determine these scores. The percentage of selected cells varied between 0.02 and 0.08 (*dashed line* in Fig. 5). Subjective inspection of these selected cells showed a slight indication of an S-shape in bins with $L > 12$ μm (*continuous line* in Fig. 5). In these bins, the nonselected cells showed a continuum of shapes between those selected and shapes with reflection symmetry. In bins with $L < 12$ μm, the cells did not show an S-shape. Two examples, one with small and one with large *L*, are shown in Fig. 6. Please note that the observed S-shapes are mirror-inverted with respect to the letter *S*.

The static shape of capsules is determined by the dimensionless ratio of bending to shear stiffness of their membrane (K_b, see Models without Shape Restrictions) and the respective RCs. In TT red cells the viscosities play an additional role, at least for the two lower values of η_0 (20). The influence of K_b is demonstrated by the model of Huang et al. (17). Unlike the red cell, its membrane is compressible. Nevertheless, their Fig. 10 clearly shows that an increase of K_b suppresses the formation of an S-shape. In the red cell models (13,14,18,19), S-shapes appear in a certain phase of the TT cycle, a signature of the RC in shear.

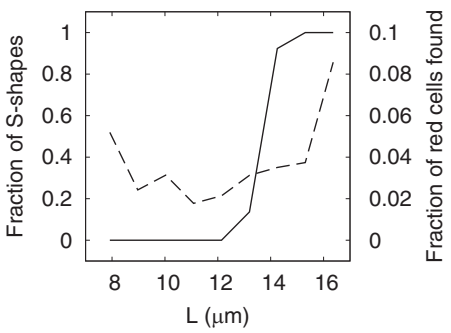

FIGURE 5 Fractions of red cells versus *L*. (*Dashed line* and *right ordinate*) Cells having low reflection symmetries but a high symmetry upon a rotation by 180°. Within these cells, the fraction showing subjectively an S-shape is shown (*continuous line* and *left ordinate*).

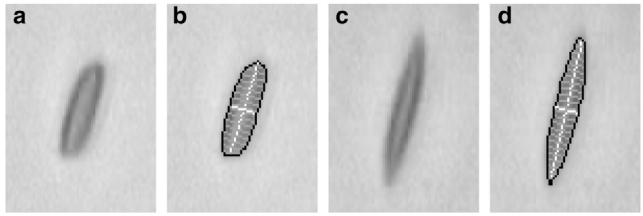

FIGURE 6 Microscopic images of red cells. (*a* and *b*) No indication of an S-shape ($\eta_0 = 55.9$ mPas, $\dot{\gamma} = 5.82$/s). (*c* and *d*) Slight indication of an S-shape ($\eta_0 = 104$ mPas, $\dot{\gamma} = 50.3$/s). The height of the images corresponds to 23.1 μm.

For the rare observation of S-shapes in our experiments (Fig. 5, *dotted line*) we suggest two sources: 1) K_b is low enough in a small percentage of the population, and/or 2) an S-shape shows up only during a certain phase during TT.

Comparisons

Choice of temperature

These data were performed at room temperature. The same applies to other experimental results to which we compare ours. For the comparison to model results, three intrinsic red cell quantities are required: the shear modulus of the red cell membrane (G_s), η_0, and the viscosity of the red cell cytoplasm (η_{cyt}). Measurements of G_s and η_0 are available at room temperature. For η_{cyt}, only measurements at 37°C exist. To remain consistent, we assume for η_{cyt} the same temperature dependence as that of water and use $\eta_{cyt} = 10$ mPas (21).

Previous experiments

Abkarian et al. (6) studied TT red cells along the undisturbed vorticity of a Poiseuille flow. Fig. 7 *b* (Δ) shows several values of $\langle\theta\rangle$ of the same individual red cell. Fig. 7 *c* (Δ) shows single values of $\langle\theta\rangle$ of two different red cells. Except for the cell at $\dot{\gamma} = 6.6$/s in Fig. 7 *c*, $\dot{\gamma}$ -values are lower than $\dot{\gamma}_t$ determined by Fischer and Korzeniewski (11). Because their value represents a population average, TT of some cells below that value is not excluded. Therefore the data of Abkarian et al. (6) are in line with our experiments (*shaded*), except for the cell at $\dot{\gamma} = 6.6$/s in Fig. 7 *c*.

The true extent of SW, hidden in our θ-histograms, is not known. We take $2\sigma_e$ as an upper bound for the respective SWR (see Section S3.2 in the Supporting Material). These values are shown in Fig. 8 by the shaded area.

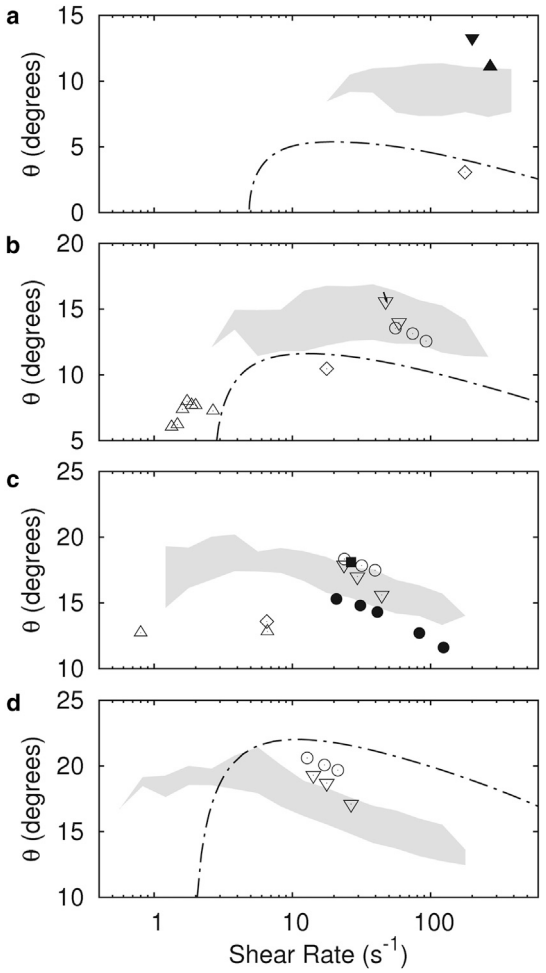

FIGURE 7 Comparison of our results with data from the literature. (*Shaded regions*) Experimental values of θ shown in Fig. 3 with η_0 in mPas: (*a*) 10.7, (*b*) 23.9, (*c*) 55.9, and (*d*) 104. (*b* and *c*, *open up-triangle*) Experimental observations (6). (*a–d*) Model results of $(\theta_{max} + \theta_{min})/2$ of a standard red cell. (*Dash-dotted lines* (24), *open down-triangle* (13), *open diamond* (26), *open circle* (27), *solid square* (17), *solid circle* (18), *solid up-triangle* (29), *solid down-triangle* (30), and *arrow* (28).) Please note that the arrow in *b* is very short and overlaps the topmost triangle.

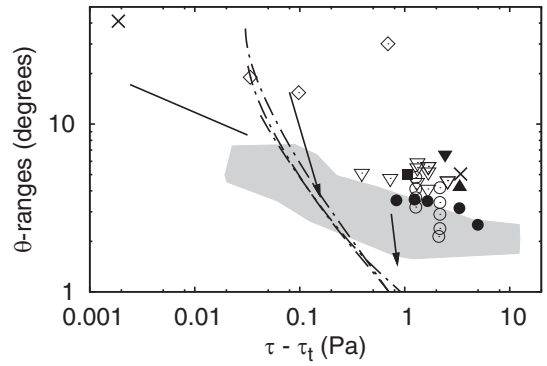

FIGURE 8 Comparison of our results with data from the literature. (*Shaded region*) Observed values of $2\sigma_e$ (Fig. 4 *a*). (*Continuous line*) Experimental observations of SWR (6). Model results of SWR from the literature. (*Dash-dotted lines* (24), *open down-triangle* (13), *open diamond* (26), *open circle* (27), *solid square* (17), *solid circle* (18), *solid up-triangle* (29), *solid down-triangle* (30), *cross* (34), and *arrows* (28).) Arrows connect models with different RCs in shear (foot, biconcave; head, almost spherical).

In the experiments of Abkarian et al. (6), $\dot{\gamma}_t$ was different when the threshold was approached by increasing or decreasing $\dot{\gamma}$, thus giving rise to a region of hysteresis. We used the value in the middle of this region to determine τ_t. The continuous line in Fig. 8 represents a fit to several SWRs of an individual red cell (6). As a result of a single red cell, it is in keeping with our experiments.

Models with shape restrictions

Keller and Skalak (5) building on previous works (22,23) described the kinematics of TT triaxial ellipsoids with a viscous interior and an inviscid membrane without elastic properties (KS model). The major axis was restricted to reside in the shear plane. Points on the surface were assumed to move in planes orthogonal to the undisturbed vorticity. The motion of the ellipsoids was determined by equilibrium and energy considerations.

Skotheim and Secomb (7) upgraded the KS model accounting for E_0, the elastic energy cyclically stored in the TT membrane. Their analysis was restricted to an oblate ellipsoid, thus describing the situation at $\dot{\gamma}_t$. Noguchi (24) added elongation and accounted for η_{mem}. His results are presented as functions of $\dot{\gamma}^* = \dot{\gamma}\eta_0 R_0/G_s$, $\lambda = \eta_{cyt}/\eta_0$, and $\eta_{mem} = 10^{-7}$ Ns/m, where $R_0 = (S/4\pi)^{1/2}$, the surface area is $S = 135\ \mu m^2$, and the shear modulus is $G_s = 6\ \mu$N/m. From his values of λ and $\dot{\gamma}^*$, we calculated η_0 and $\dot{\gamma}$ using $\eta_{cyt} = 10$ mPas. For τ_t we used his midrange values between TB and TT. His results of $\langle\theta\rangle$ are shown as dash-dotted lines in Fig. 7, *a*, *b*, and *d*. In keeping with our observations, his data show an increase of $\langle\theta\rangle$ with η_0 and a nonmonotonic behavior. In contrast to our data, his effects are much stronger. Similarly, his SWRs (*dash-dotted lines* in Fig. 8) depend much more on $\tau - \tau_t$ than does our data.

Vlahovska et al. (25) considered a capsule model with an incompressible, shear elastic membrane, and an unstressed RC. A direct comparison of this model to our data is not possible because its shape is almost spherical and the values of λ are much greater than ours. However, we note that these authors also found a nonmonotonic behavior of $\langle\theta\rangle$ as a function of $\dot{\gamma}$.

Models without shape restrictions

In models without shape restrictions, the membrane is represented as a collection of points forming the vertices of a subdivision of the red cell surface. Two types of models exist with respect to the inclusion of the properties of the membrane skeleton. In the first type, a two-dimensional continuum mechanical description is replaced by discretized representation. The results are given in dependence of a few dimensionless parameters. The second type would

be so-called multiscale models that start from the elasticity of the basic building elements of the membrane skeleton. Their results usually depend on physical quantities.

Because our values of θ depend weakly on η_0, we use model results for comparison provided that $0.7 < \eta_0^{\text{model}}/\eta_0^{\text{experiment}} < 1.3$. Under this restriction, we compare $\langle\theta\rangle$ of six and SWR of seven first-type models to our results (13,17,18,26–28). One second-type model is compared to both quantities (29,30). All these models except one (28) use exclusively a biconcave stress-free shape as RC in shear. The second-type model, but none of the first-type models, accounts for η_{mem}. All first-type models use the same constitutive equation for the two-dimensional shear elasticity (31). The effective constitutive equation of the second-type model is not known.

In the first-type models, the results are given as functions of λ, $\text{Ca} = \tau a_0/G_s$, and in some models by $K_b = \kappa_b/{a_0}^2 G_s$, where $a_0 = (3V/4\pi)^{1/3}$, V is the red cell volume, and κ_b is the bending stiffness of the membrane. With $V = 94\ \mu\text{m}^3$, η_{cyt}, and $G_s = 2.5\ \mu\text{N/m}$ (32), we calculated the values of η_0, $\dot{\gamma}$, and when applicable, of κ_b.

To compensate for the absent membrane viscosity in first-type models, we used $\eta_{\text{cyt}} > 10$ mPas. For models providing values of $\dot{\gamma}_t$, the value of η_{cyt} was obtained by a comparison of the theoretical and experimental values of $\dot{\gamma}_t$ (11,13,26,28). For the other models (17,18,27), $\eta_{\text{cyt}} =$ 40 mPas was used (see Table 2). Without the increase of η_{cyt}, the model values of $\langle\theta\rangle$ are greater than the experimental values. The increase of η_{cyt} increases η_0 and thanks to the experimental increase of θ with η_0, the agreement improves. This is demonstrated in Section 3.1 in the Supporting Material.

To begin, we compare the values of $\langle\theta\rangle$. Most model results are close to the experimental data (Fig. 7). In two models, $\langle\theta\rangle$ is given at three different values of η_0 (13,27). These data show a steeper dependence on η_0 than observed. In none of the models does the range of $\dot{\gamma}$ covered allow a comparison with the observed nonmonotonic behavior.

The values of Sui et al. (18) are below the shaded area (Fig. 7 *c*). Two causes can be put forward: First, their gap width is the smallest (see Table 2). Based on a vesicle model (33), approximately half the difference between the data in Sui et al. (18) and those in Huang et al. (17) or Dodson and Dimitrakopoulos (27) can be ascribed to confinement. Second, θ is defined as the inclination of the maximum length of the TT red cell. In the case of S-shapes, θ is therefore lower than in the other models, which use the inertia tensor to determine θ.

TABLE 2 Parameters of first-type models

η_{cyt}/mPas	d_w/μm	$\kappa_b/10^{-19}$ J	c_0a_0	SFS	Symbol	Reference
30	18	4	−2.09	Biconcave	▽	(13)
19.4	18	4	−2.09	Biconcave	↓	(28)
18.4	18	6	4	Spheroid	↓	(28)
50	28	4	0	Biconcave	◇	(26)
40	∞	0	NA	Biconcave	○	(27)
40	28	0	NA	Biconcave	■	(17)
40	14	0	NA	Biconcave	●	(18)
NR	∞	6.8	0	Biconcave	×	(34)

The cytoplasmic viscosity (η_{cyt}) is increased to account for the viscosity of the membrane. The value d_w is the size of the fluid box in the direction of the undisturbed gradient. *SFS*, stress-free shape; Spheroid is an oblate spheroid with a ratio of minor to major axes of 0.9; NR, not relevant; NA, not applicable.

The values of Le and Tan (26) are considerably below our values (Fig. 7, *a–c*). We have no explanation for this discrepancy. Their SWRs reach down to very small, and in one case out of three, to negative values of θ. In contrast, even in our outliers we observed negative values only very rarely (Fig. S7).

To compare the SWRs, the values of τ_t of the models are calculated from the capillary numbers at the threshold that are given in four models (13,26,28,34). For the other models, the experimental value of τ_t (11) is used. Because the values of SWR do not depend explicitly on η_0, we use model results for $7.5\ \text{mPas} < \eta_0 < 200$ mPas.

Most model-SWRs with biconcave stress-free shapes are above the shaded area in Fig. 8, which represents an upper bound of the population. The models, on the other hand, describe a standard red cell. Therefore, their SWRs appear to be too large. Choosing a stress-free shape close to the sphere reduced model-SWRs appreciably (*arrows* in Fig. 8 and Table 2).

A comparison of the dependence of model-SWRs on $\tau-\tau_t$ with the observed trend of σ_e requires that the model data cover a large enough range of $\tau-\tau_t$. Of all models considered here, this applies to one model (26) only. Its data, however, are not in keeping with the observed decrease of σ_e with increase of $\tau-\tau_t$ (Fig. 8). If we exclude the data point at $\tau-\tau_t = 0.67$ Pa and consider all models with biconcave stress-free shapes, the combined trend is in accord with the observed one.

Two cases of a second-type model are shown in Figs. 7 *a* and 8 (*solid triangles*). The cases differ in the value of η_{cyt}: 6 and 13 mPas in Peng et al. (29) and Peng and Zhu (30), respectively. As expected, the impact of this difference is small because the energy dissipation in TT red cells is dominated by η_{mem} (35). The model values are somewhat above the experimental data.

CONCLUSIONS

The situation of isolated red cells in viscous solutions differs in two ways from the situation in the circulation. First, the viscosity of blood plasma is ~2 mPas (at room temperature). Second, the red cells are crowded in large vessels or confined in small vessels. In these respects, our experiments have no direct relevance for the situation in the circulation. However, the boundary conditions for the red cells in our experiment are well controlled and can be modeled with great precision. The fit of these models to the experiments

can help to improve our knowledge of the mechanical properties of the red cell. Besides the principal interest in these properties, this information can be used to model the physiological situation.

To compensate for the lack of η_{mem} in the first-type models, we increased η_{cyt} by a constant factor in comparing our experimental results to their theory. However, as an addition of η_{mem} to the KS-model (21) indicates, this factor should at least depend on the shape of the deformed red cell (36). Therefore, it can be expected that an explicit account of η_{mem} in first-type models will improve the agreement. A fit of η_{mem} to the dependence of θ on $\dot{\gamma}$ and η_0 (Figs. 3 and S7) may even allow, by future modeling, us to determine a possible dependence of η_{mem} on the two-dimensional membrane shear rate. This expectation warrants the use of large ranges of $\dot{\gamma}$ and η_0, even if they are not directly related to the situation in vivo.

Another challenge, besides the inclusion of η_{mem}, is to find an appropriate RC in shear. These data do not support a biconcave stress-free shape (Fig. 8 and Discussion in Section S4.4 in the Supporting Material). A spherical stress-free shape is excluded because it was shown that the membrane has a configuration of minimal shear elastic energy (2). Three models exist that use stress-free shapes between the biconcave disk and the sphere (28,34,37–39). Their stress-free shapes are different, and in addition, different flow situations were modeled. To reach a consensus on this issue requires 1) to model different flow situations that critically depend on the RC in shear, 2) to test the same flow situation with different RCs, and 3) to make more experiments that are appropriate for this test; among these are the collection of statistical firm data on the amplitudes of L and θ during SW. In the end, it may become necessary to consider the general concept of an RC in which no stress-free shape exists at all. We expect that an RC according to this general concept will widen our understanding of the physiology of the red cell.

SUPPORTING MATERIAL

Supporting Materials and Methods, Supporting Results and Discussion, and 17 figures are available at http://www.biophysj.org/biophysj/supplemental/S0006-3495(15)00122-8.

AUTHOR CONTRIBUTIONS

T.M.F. designed the research, performed the research, analyzed the data, and wrote the manuscript. R.K. performed the research and contributed analytic tools.

ACKNOWLEDGMENTS

The authors thank the staff of the blood bank, Universitätsklinikum Aachen, for their cooperation in placing the blood samples at our disposal; the staff of the mechanical workshop, Universitätsklinikum Aachen, for helping along the way; Dipl. Ing. M. Laumen, RWTH-Aachen, for the opportunity to perform the viscometric measurements in his laboratory; and Dr. Le, Institute of High Performance Computing, Singapore, and Drs. Yazdani and Bagchi, Department of Mechanical and Aerospace Engineering, Rutgers University, Piscataway, New Jersey, for communicating details of their published results. The capillaries were a gracious sample delivery from Hilgenberg, Malsfeld, Germany.

SUPPORTING CITATIONS

References (40–44) appear in the Supporting Material.

REFERENCES

1. Fischer, T. M., C. W. M. Haest, …, R. Skalak. 1981. The stress-free shape of the red blood cell membrane. *Biophys. J.* 34:409–422.
2. Fischer, T. M. 2004. Shape memory of human red blood cells. *Biophys. J.* 86:3304–3313.
3. Fischer, T., and H. Schmid-Schönbein. 1977. Tank tread motion of red cell membranes in viscometric flow: behavior of intracellular and extracellular markers (with film). *Blood Cells.* 3:351–365.
4. Schmid-Schöenbein, H., and R. Wells. 1969. Fluid drop-like transition of erythrocytes under shear. *Science.* 165:288–291.
5. Keller, S. R., and R. Skalak. 1982. Motion of a tank-treading ellipsoidal particle in a shear flow. *J. Fluid Mech.* 120:27–47.
6. Abkarian, M., M. Faivre, and A. Viallat. 2007. Swinging of red blood cells under shear flow. *Phys. Rev. Lett.* 98:188302.
7. Skotheim, J. M., and T. W. Secomb. 2007. Red blood cells and other nonspherical capsules in shear flow: oscillatory dynamics and the tank-treading-to-tumbling transition. *Phys. Rev. Lett.* 98:078301.
8. Mazeron, P., S. Muller, and H. el Azouzi. 1997. Deformation of erythrocytes under shear: a small-angle light scattering study. *Biorheology.* 34:99–110.
9. Fischer, T. M. 2010. A method to prepare isotonic dextran-salt solutions. *Cytometry A.* 77:805–810.
10. Deuticke, B. 1968. Transformation and restoration of biconcave shape of human erythrocytes induced by amphiphilic agents and changes of ionic environment. *Biochim. Biophys. Acta.* 163:494–500.
11. Fischer, T. M., and R. Korzeniewski. 2013. Threshold shear stress for the transition between tumbling and tank-treading of red blood cells in shear flow: dependence on the viscosity of the suspending medium. *J. Fluid Mech.* 736:351–365.
12. Misbah, C. 2006. Vacillating breathing and tumbling of vesicles under shear flow. *Phys. Rev. Lett.* 96:028104.
13. Yazdani, A. Z. K., and P. Bagchi. 2011. Phase diagram and breathing dynamics of a single red blood cell and a biconcave capsule in dilute shear flow. *Phys. Rev. E Stat. Nonlin. Soft Matter Phys.* 84:026314.
14. Omori, T., T. Ishikawa, …, T. Yamaguchi. 2012. Tension of red blood cell membrane in simple shear flow. *Phys. Rev. E Stat. Nonlin. Soft Matter Phys.* 86:056321.
15. Rumscheidt, F. D., and S. G. Mason. 1961. XII. Deformation and burst of fluid drops in shear and hyperbolic flow. *J. Colloid Sci.* 16:238–261.
16. Mottaghy, K., G. Driessen, …, H. Schmid-Schönbein. 1977. The floating-droplets oxygenator: developments using fluorocarbons with coaxial rotating cylinders. *Trans. Am. Soc. Artif. Intern. Organs.* 23:464–469.
17. Huang, W.-X., C. B. Chang, and H. J. Sung. 2012. Three-dimensional simulation of elastic capsules in shear flow by the penalty immersed boundary method. *J. Comput. Phys.* 231:3340–3364.
18. Sui, Y., Y. T. Chew, …, H. T. Low. 2008. Dynamic motion of red blood cells in simple shear flow. *Phys. Fluids.* 20:112106.
19. Shi, X., G. Lin, …, D. A. Fedosov. 2013. A lattice Boltzmann fictitious domain method for modeling red blood cell deformation and multiple-cell hydrodynamic interactions in flow. *Int. J. Numer. Methods Fluids.* 72:895–911.

20. Fischer, T. M., and R. Korzeniewski. 2011. Effects of shear rate and suspending medium viscosity on elongation of red cells tank-treading in shear flow. *Cytometry A.* 79:946–951.

21. Tran-Son-Tay, R., S. P. Sutera, and P. R. Rao. 1984. Determination of red blood cell membrane viscosity from rheoscopic observations of tank-treading motion. *Biophys. J.* 46:65–72.

22. Jeffery, G. B. 1922. The motion of ellipsoidal particles immersed in a viscous fluid. *Proc. R. Soc. Lond. A. Biol. Sci.* 102:161–179.

23. Roscoe, R. 1967. On the rheology of a suspension of viscoelastic spheres in a viscous liquid. *J. Fluid Mech.* 28:273–293.

24. Noguchi, H. 2009. Swinging and synchronized rotations of red blood cells in simple shear flow. *Phys. Rev. E Stat. Nonlin. Soft Matter Phys.* 80:021902.

25. Vlahovska, P. M., Y.-N. Young, …, C. Misbah. 2011. Dynamics of a non-spherical microcapsule with incompressible interface in shear flow. *J. Fluid Mech.* 678:221–247.

26. Le, D. V., and Z. Tan. 2014. Hydrodynamic interaction of elastic capsules in bounded shear flow. *Commun. Comput. Phys.* 16:1031–1055.

27. Dodson, 3rd, W. R., and P. Dimitrakopoulos. 2011. Oscillatory tank-treading motion of erythrocytes in shear flows. *Phys. Rev. E Stat. Nonlin. Soft Matter Phys.* 84:011913.

28. Cordasco, D., A. Yazdani, and P. Bagchi. 2014. Comparison of erythrocyte dynamics in shear flow under different stress-free configurations. *Phys. Fluids.* 26:041902.

29. Peng, Z., R. J. Asaro, and Q. Zhu. 2011. Multiscale modeling of erythrocytes in Stokes flow. *J. Fluid Mech.* 686:299–337.

30. Peng, Z., and Q. Zhu. 2013. Deformation of the erythrocyte cytoskeleton in tank treading motions. *Soft Matter.* 9:7617–7627.

31. Skalak, R., A. Tözeren, …, S. Chien. 1973. Strain energy function of red blood cell membranes. *Biophys. J.* 13:245–264.

32. Dimitrakopoulos, P. 2012. Analysis of the variation in the determination of the shear modulus of the erythrocyte membrane: effects of the constitutive law and membrane modeling. *Phys. Rev. E Stat. Nonlin. Soft Matter Phys.* 85:041917.

33. Luo, Z. Y., S. Q. Wang, …, B. F. Bai. 2013. Inertia-dependent dynamics of three-dimensional vesicles and red blood cells in shear flow. *Soft Matter.* 9:9651–9660.

34. Tsubota, K.-i., S. Wada, and H. Liu. 2013. Elastic behavior of a red blood cell with the membrane's nonuniform natural state: equilibrium shape, motion transition under shear flow, and elongation during tank-treading motion. *Biomech. Model. Mechanobiol.* 13:735–746.

35. Secomb, T. W., and R. Skalak. 1982. Surface flow of viscoelastic membranes in viscous fluids. *Quart. J. Mech. Appl. Math.* 35:233–247.

36. Noguchi, H., and G. Gompper. 2005. Dynamics of fluid vesicles in shear flow: effect of membrane viscosity and thermal fluctuations. *Phys. Rev. E Stat. Nonlin. Soft Matter Phys.* 72:011901.

37. Tsubota, K.-i., and S. Wada. 2010. Elastic force of red blood cell membrane during tank-treading motion: consideration of the membrane's natural state. *Int. J. Mech. Sci.* 52:356–364.

38. Cordasco, D., and P. Bagchi. 2013. Orbital drift of capsules and red blood cells in shear flow. *Phys. Fluids.* 25:091902.

39. Peng, Z., A. Mashayekh, and Q. Zhu. 2014. Erythrocyte responses in low-shear-rate flows: effects of non-biconcave stress-free state in the cytoskeleton. *J. Fluid Mech.* 742:96–118.

40. Lindert, J., J. Werner, …, A. R. Pries. 2002. OPS imaging of human microcirculation: a short technical report. *J. Vasc. Res.* 39:368–372.

41. Happel, J., and H. Brenner. 1983. Low Reynolds Number Hydrodynamics. Martinus Nijhoff, The Hague, The Netherlands.

42. Bransky, A., N. Korin, …, U. Dinnar. 2007. The rheologic properties of erythrocytes: a study using an automated rheoscope. *Rheol. Acta.* 46:621–627.

43. Sutera, S. P., and R. Tran-Son-Tay. 1983. Mathematical model of the velocity field external to a tank-treading red cell. *Biorheology.* 20:267–282.

44. Fischer, T. M. 2007. Tank-tread frequency of the red cell membrane: dependence on the viscosity of the suspending medium. *Biophys. J.* 93:2553–2561.